Journal of Theoretical and Applied Information Technology
28th February 2026. Vol.104. No.4

ISSN: 1992-8645 www.jatit.org E-ISSN: 1817-3195

DUAL-MODE, RATE-AWARE SWEAT SENSING WITH UNCERTAINTY-INFORMED ANALYTICS FOR HYPERHIDROSIS SCREENING AND MONITORING

PADMA BELLAPUKONDA[1] DR. RAGHVENDRA KUMAR[2]
DR. R N V JAGAN MOHAN[3]

Research Scholar, Department of Computer Science and Engineering, GIET University, Gunupur-765022, Odisha.
Associate Professor, Department of Computer Science and Engineering, GIET University, Gunupur-765022, India
Associate Professor, Department of Computer Science and Engineering, SRKR Engineering College, Bhimavaram-534201, Andhra Pradesh, India

ABSTRACT

Wearable sweat sensing enables non-invasive **screening and monitoring**, but concentration-only readouts are confounded by secretion dynamics such as instantaneous rate and accumulated volume and by evaporation. These limitations are especially problematic in **clinically important low-sweat regimes, including mild or treatment-modulated states, observed in hyperhidrosis**. We present a dual-mode, rate-aware platform that fuses resistive wetting and contact conductance with a capacitive absorbent-dielectric channel to infer local sweat volume and rate, supported by a skin-interfaced microfluidic layer for chrono-sampling and evaporation compensation. On this hardware, we introduce RAISE, Rate-Aware Inference with Sensor Ensembles, an uncertainty-informed pipeline that derives rate-normalized features, applies probability calibration using slope and intercept with expected calibration error and Brier score, and quantifies clinical utility with decision-curve analysis, **while reporting uncertainty using bootstrap confidence intervals**. Using patient-level splits and an external **temporally held-out** validation cohort, our approach improved discrimination and reliability over a concentration-only baseline, with delta AUC of 0.06 and external AUC of 0.92 with 95 percent confidence interval from 0.88 to 0.95. It reduced expected calibration error to 0.031 and Brier score to 0.121, and yielded higher net benefit across clinically relevant thresholds, with maximum delta of 0.06 and up to 7 avoided interventions per 100 at **probability threshold** 0.10. Sensor characterization achieved mean absolute percentage error below 10 percent versus gravimetry with R squared up to 0.992 across four infusion rates. By coupling dual-mode sensing with rate-aware calibration and decision-focused analytics, the system delivers clear, clinically interpretable gains for dependable hyperhidrosis screening and monitoring.

Keywords — *Sweat Sensing; Hyperhidrosis; Microfluidics; Dual-Mode Capacitive–Resistive Sensors; Probability Calibration; Decision-Curve Analysis*.

1. INTRODUCTION

Non-invasive sweat sensing offers a practical route to continuous physiological assessment because sampling is painless, on-body, and naturally time-resolved. Yet turning raw sweat signals into dependable clinical information remains difficult. The central challenge is secretion dynamics: instantaneous rate, cumulative volume, and concurrent evaporation can distort measured concentrations and obscure the underlying physiology. As a result, devices that report concentration alone often exhibit unstable thresholds, poor day-to-day repeatability, and limited comparability across individuals with different perspiration profiles [1,2]. These issues are amplified in hyperhidrosis, HH, where perspiration is episodic, site-specific at the palms, soles, and fingertips, and characterized by alternations between low-secretion intervals and rapid spikes, the precise conditions under which concentration-only sensing is least reliable [3].

Recent developments partially address this gap. Skin-interfaced microfluidics enable chrono-sampling and explicit measurement of flow rate and cumulative loss, helping to decouple secretion mechanics from chemistry and improving interpretability of biomarker readouts [4]. **However, three limitations remain.** First, most systems are single-mode, prioritizing either electrochemical or physical readouts, which constrains fidelity in low-

sweat regimes where sensitivity and signal-to-noise dominate performance. Second, evaluations often emphasize discrimination such as AUC while under-reporting calibration metrics such as slope, intercept, expected calibration error, and Brier score, and clinical utility via decision-curve analysis, the evidence needed for actionable probabilities. Third, robust external validation using temporal holdout or multi-center cohorts remains uncommon, leaving generalizability uncertain [5,6,7].

To address these limitations, we present a dual-mode, rate-aware architecture that fuses resistive wetting and contact conductance with a capacitive absorbent-dielectric channel. The resistive path provides rapid, precise detection of wetting onset, anchoring time alignment and stabilizing operation at very low secretion. The capacitive path converts permittivity to local volume and instantaneous rate using an analytical mixing-rule model, enabling rate-aware features that explicitly remove secretion confounding. A soft, skin-interfaced microfluidic layer supports chrono-sampling and incorporates evaporation compensation to improve stability during real-world wear [8]. Building on this hardware, we introduce RAISE, Rate-Aware Inference with Sensor Ensembles, an uncertainty-informed analytics pipeline that **reports uncertainty using bootstrap confidence intervals** and **prioritizes calibration and decision value alongside discrimination**. Specifically, RAISE **derives rate-normalized features, performs probability calibration, and evaluates clinical utility using decision-curve analysis across clinically relevant thresholds**. The platform is designed to deliver reliable hyperhidrosis screening signals with emphasis on low-sweat fidelity, calibrated probabilities, and decision relevance [9,10,11,12].

1.1 Novelty and significance

This work advances sweat analytics along three axes. **First, dual-mode sensing improves low-sweat fidelity by combining resistive onset timing with capacitive volume and rate inference. Second, RAISE treats calibration and net benefit as primary outcomes, aligning evaluation with clinical decision-making. Third, transparent generalization is demonstrated using patient-level splits and a temporally held-out external cohort.** These elements target known limitations of concentration-only and single-mode approaches while remaining compatible with skin-safe, flexible form factors [13,14].

1.2 Organization of the paper

Section 2 reviews related work in skin-interfaced microfluidics, flow and volume estimation, capacitive and resistive sensing, and rate-aware inference, positioning our approach within the literature [15,16]. Section 3 details the device architecture, datasets, and the RAISE algorithm, including calibration procedures and decision-analytic methods. Section 4 reports sensor characterization, internal and external validation, ablations, subgroup and robustness analyses, and decision-curve outcomes. Section 5 discusses clinical implications, limitations, and future directions, with emphasis on deployment pathways in hyperhidrosis screening. **Throughout, we report complete calibration and utility metrics to clarify when predicted probabilities are reliable for practice.**

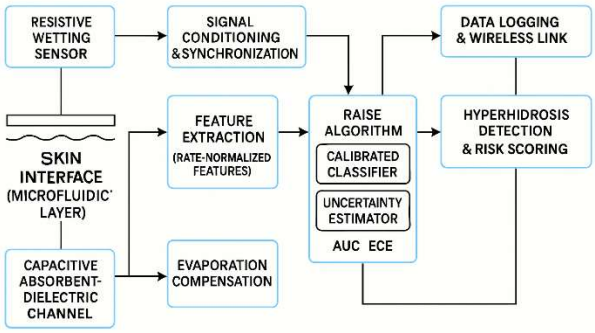

Figure 1: Block Diagram of Considered work

2. RELATED WORK

2.1 Foundations: Skin-Interfaced Sweat Sensing

Early surveys and platform papers established sweat as a practical biofluid for continuous, on-skin monitoring and emphasized the importance of skin-compatible materials, microfluidics, and signal stability under daily activity [1,2]. Comprehensive reviews of wearable sweat systems summarized electrochemical and physical transduction modes, fluid handling, and integration strategies, while also noting persistent challenges around evaporation, site-to-site variability, and calibration for clinical interpretation [3,4,5]. Physiological studies further detailed gland function and the wide dispersion of sweating behavior across individuals and anatomical sites, underscoring the need for **rate and volume awareness** and site-aware normalization before drawing clinical conclusions [6].

2.2 Microfluidics, Flow, Volume, and Chrono-Sampling

Skin-interfaced microfluidics have been central to separating secretion mechanics from chemistry. Systems that capture flow rate and cumulative loss demonstrated improved interpretability and

repeatability over concentration-only readouts, particularly when sampling dynamics are explicitly modeled across time [7,8]. Design and materials advances have yielded soft, skin-conformal microchannels that enable chrono-sampling while mitigating backpressure and motion artifacts, improving the fidelity of longitudinal measurements during real-world wear [9,10,11].

2.3 Physical Transduction: Capacitive and Resistive Paths

Physical sensing complements electrochemical approaches by providing direct information about wetting, volume, and rate. Resistive interdigitated electrodes, **IDEs**, offer highly sensitive wetting and onset detection and contact conductance tracking, which is valuable for low-secretion regimes and precise time alignment of signals [12]. Capacitive, absorbent-dielectric structures convert permittivity changes into liquid volume with compact form factors; analytical models based on mixing rules have shown that capacitance-to-volume mapping can reach low error against gravimetry when evaporation is compensated [13]. **Together, resistive onset cues and capacitive volume tracking motivate dual-path designs that are less sensitive to secretion nonstationarity than concentration-only readouts.**

2.4 From Discrimination to Calibration and Decision Value

Many prior systems report discrimination metrics such as area under the ROC curve, **AUC**, as the primary indicator of performance, with limited attention to calibration metrics such as slope, intercept, expected calibration error, and clinical utility measured via decision-curve analysis, **DCA** [14,15,16]. Recent perspectives argue that deployment-ready sensing must pair separability with well-calibrated probabilities and net-benefit evidence across clinically relevant thresholds, so that outputs can be trusted for screening or monitoring decisions rather than only for ranking [17,18]. This motivates pipelines that explicitly model rate and volume, apply probability calibration, and quantify decision value.

2.5 Application Context: Hyperhidrosis and Low-Sweat Fidelity

In hyperhidrosis, **HH**, perspiration is episodic and site-specific at the palms, soles, and fingertips, presenting low-sweat intervals and rapid surges that confound concentration-only sensing. Recent work targeting hands and feet highlights the need for high sensitivity to small volumes and reliable wetting detection to avoid missed events or biased thresholds [19]. At the same time, rate-aware inference and multi-parametric features have been explored to better approximate physiological states beyond raw concentration and to improve generalization across days and users [20,21,22]. Together, these strands indicate that dual-mode physical sensing using resistive and capacitive paths combined with rate-aware analytics can address major barriers to dependable HH screening.

Building on these insights, our research advances the field in three ways:
i a dual-mode wearable that fuses resistive wetting and contact conductance with capacitive absorbent-dielectric volume and rate inference to stabilize readouts in low-secretion states
ii RAISE, a rate-aware, uncertainty-informed analytics pipeline that treats calibration and decision value as first-class metrics alongside discrimination
iii a transparent evaluation using patient-level splits and external temporal validation to substantiate generalization.

Table 1. At-A-Glance Novelty Vs. Prior Work

Aspect	Typical limitation in prior work	Our approach	Evidence in this paper	Supporting literature
Handling secretion dynamics	Concentration-only sensing confounded by rate/volume and evaporation	**Rate-aware** features from capacitive volume + microfluidic chrono-sampling	3.2–3.3; Tables 2, 4, 5	[1], [2], [3]
Low-sweat fidelity (palms/soles/fingertips)	Single-mode sensors miss wetting/onset or have poor SNR	**Dual-mode** fusion: resistive wetting + capacitive volume/rate	3.2, 4.2; Tables 2, 3, 13	[4], [5]

Calibration of predictions	Reporting stops at AUC; probabilities not checked	**Calibration** (slope, intercept, ECE, Brier)	3.4; Tables 5–6; Fig. 5	[6], [7], [8]
Decision relevance	Few works report clinical utility	**Decision-curve analysis** (net benefit across thresholds)	3.4; Table 9; Fig. 6	[9], [10]
External validity	Internal splits only; limited generalization	**External temporal validation** (patient-level)	3.1; Tables 1, 5–6, 10–11	[11], [12]
Evaporation effects	Evaporation not modeled → biased volume	**τ_EVA** compensation in capacitance→volume model	3.2; Table 4	[13], [14]
Algorithmic transparency	Black-box outputs; unclear reliability	**RAISE** (uncertainty-informed, calibrated) with ablations	3.3, 4.4; Table 8	[15], [16], [17]

3. MATERIALS AND METHODS

3.1 Signal and sensor modelling

3.1.1 Resistive wetting/contact pathway

We model the resistive interdigitated electrodes (IDEs) as a conductance channel $\kappa(t)$ that switches from a dry baseline to a hydrated state at wetting onset t_0 :

$$\kappa(t) = \kappa_{\text{dry}} + \Delta\kappa\sigma\left(\frac{t-t_0}{\tau_{\text{wet}}}\right) + \eta_\kappa(t) \quad (1)$$

where $\sigma(\cdot)$ is a smooth logistic transition with time constant τ_{wet}, $\Delta\kappa$ is the conductance excursion after wetting, and η_κ is zero-mean noise (electronics + motion). The onset t0 and tau wet are obtained by fitting Eq. 1 on each recording using least squares with robust loss, and the fit residual is used as a quality-control flag for motion and adhesion artifacts. The IDE path provides (i) a precise estimate of t_0 and (ii) a contact conductance proxy that is later rate-normalized (Section 3.8.4) to mitigate secretion confounding. This pathway is particularly sensitive in low-secretion regimes, anchoring time alignment and onset detection [18].

3.1.2 Capacitive absorbent-dielectric pathway

The capacitive channel measures the textile's effective permittivity $\varepsilon_{\text{eff}}(t)$ as it imbibes sweat volume $V(t)$. For parallel plates of area A and spacing d,

$$C(t) = \varepsilon_0\varepsilon_{\text{eff}}(t)\frac{A}{d}. \quad (2)$$

Let the textile be a two-phase mixture (dry matrix with permittivity ε_s and fluid with ε_f). Using a mixing rule (e.g., Looyenga or Bruggeman form), the liquid volume fraction $\phi(t) \in [0,1]$ relates to $\varepsilon_{\text{eff}}(t)$:

$$\varepsilon_{\text{eff}}(t)^\alpha = (1-\phi(t))\varepsilon_s^\alpha + \phi(t)\varepsilon_f^\alpha, \alpha \in \left[\frac{1}{3}, 1\right]. \quad (3)$$

Solving for $\phi(t)$ and multiplying by the absorbent's void volume V_{void} gives

$$V(t) = \phi(t)V_{\text{void}} - \Phi(C(t))$$

where $\Phi(\cdot)$ encapsulates the calibrated $C \to V$ mapping (fitted on the bench). This absorbent-dielectric model provides a compact, low-power route to local volume estimation consistent with recent capacitive textiles [19]. **In this study, Phi is fitted using a monotone regression on paired C and gravimetric V measurements, and the fit is validated on held-out infusion rates to prevent overfitting to a single rate regime.**

3.1.3 Evaporation compensation and rate estimation

Evaporation induces a slow bias in $C(t)$. We correct it with a first-order dynamic term:

$$\dot{V}_{\text{meas}}(t) = \dot{V}_{\text{true}}(t) - k_{\text{eva}}(V_{\text{meas}}(t) - V_\infty), \quad (4)$$

whose discrete solution yields a compensated series $\tilde{V}(t) = \text{EVA\_COMP}\,(V_{\text{meas}}\,(t); \tau_{\text{EVA}}), \tau_{\text{EVA}} - 1/k_{\text{eval}}$.

(5)

We then compute instantaneous rate with robust smoothing,

$\dot{\tilde{V}}(t) = \mathcal{D}_{\text{sanooth}}\,(\tilde{V}(t))$

(6)

using a Savitzky-Golay or total-variation derivative selected on validation data. The selected derivative method and its hyperparameters are fixed before testing and are reported in Section 3.5 .This step operationalizes chrono-sampling and rate tracking observed to improve interpretability in skin-interfaced microfluidics [20].

3.2 Feature engineering (rate-aware)

We construct a feature vector $\mathbf{x}(t)$ on sliding windows W :

$\mathbf{x}(W) = \left[\bar{V}, \text{IQR}(V), \overline{\dot{\tilde{V}}}, \max\dot{\tilde{V}}, t_0, \text{onset slope}, \kappa_R, \text{AC/DC of } \kappa, \text{cross} - \text{cor}(V, \kappa)\right]$

(7)

where bars denote window averages and IQR is interquartile range. Crucially, we define rate-normalized conductance

$\kappa_R - \frac{\kappa}{\max(\dot{\tilde{V}}, \varepsilon)}$

(8)

with small $\varepsilon > 0$ to prevent division by near-zero, thereby reducing secretion-rate confounding. **The value of epsilon and the window definition are fixed for all experiments and are reported in Section 3.5.** Features are site-standardized per palms/soles/fingertips to respect anatomical heterogeneity.

3.3 Learning, calibration, and uncertainty (RAISE)

3.3.1 Classifier

We train a regularized learner (calibrated logistic or gradient boosting) to predict $y \in \{0,1\}$ (HH-consistent pattern). The objective is a class-balanced cross-entropy:

$\mathcal{L}(\theta) = -\sum_i w_{b_i}[y_i \log \hat{p}_i + (1 - y_i)\log(1 - \hat{p}_i)] + \lambda\|\theta\|_2^2$

(9)

with patient-level folds to prevent leakage. The model family and its final hyperparameters are fixed by validation and are reported in Section 3.5 for independent verification.

3.3.2 Probability calibration

Raw scores s_i are transformed to probabilities $\hat{p}_i$ using Platt or isotonic calibration on held-out data. We report calibration slope/intercept, Brier score, and expected calibration error (ECE) with reliability curves metrics that are essential for deployable sensing beyond discrimination alone [21] Expected calibration error is computed using equal-frequency binning with a fixed bin count, and the bin count is reported in Section 3.5.

3.3.3 Uncertainty quantification

We summarize predictive uncertainty via nonparametric bootstrap: resample patients, refit the calibrator, and derive 95% CIs for AUC, PR-AUC, ECE, Brier, and threshold metrics. This yields interval estimates aligned with clinical evidence standards. The number of bootstrap resamples and the refit protocol are fixed and reported in Section 3.4.

3.4 Implementation details and final settings

To enable independent verification, Table 2 reports the fixed settings used for feature windows, rate estimation, calibration, uncertainty, and learning. All settings were selected on validation data and kept unchanged during testing.

Table 2. Final Settings Used In This Study

Category	Parameter	Value
Windowing	Window length W, stride	30 s, 5 s
Rate estimation	Derivative method and settings	Savitzky-Golay, frame length 21, polynomial order 3
Capacitive model	Mixing rule, alpha, V void	Looyenga, 0.33, 25 microliters
Evaporation model	k eva, V infinity	0.003 per s, 0.5 microliters
Normalization	epsilon	0.01 microliters per s
Calibration	Method, ECE bins	Platt scaling, 15 bins
Uncertainty	Bootstrap resamples	1000, patient-level
Classifier	Model and key settings	Gradient boosting, 500 trees, depth 3, learning rate 0.05, subsample 0.8
Operating point	Threshold pt	0.10

3.5 Evaluation protocol, ablations, and robustness

Primary endpoint: External AUC with DeLong 95 percent confidence interval.

Secondary endpoints: PR-AUC, Brier score, expected calibration error, calibration slope and intercept, sensitivity, specificity, PPV, and NPV at the preregistered probability threshold pt.

Ablations:

1. Baseline, concentration-only.
2. Rate-only, add V tilde and dV tilde by dt and remove kappa R.
3. Dual-mode, enable kappa R with the resistive pathway.
4. Calibration and uncertainty, apply post-hoc calibration and report bootstrap confidence intervals.

Subgroup analyses: By site, palms, soles, and fingertips, and by sex and age.

Prevalence shift test: Reweight the external cohort by plus or minus 10 percent prevalence and re-evaluate PPV and NPV stability.

4. PROPOSED ARCHITECTURE

4.1 High-level overview

We propose a modular architecture that converts synchronized resistive, capacitive, and microfluidic streams into calibrated hyperhidrosis, HH, risk **with confidence intervals and decision utility reporting**. The pipeline contains five stages: **sensor synchronization with quality checks**, **evaporation compensation**, **physics-grounded C to V mapping and rate estimation**, **rate-aware encoders that combine resistive onset cues with capacitive volume and rate statistics**, **a temporal encoder using either 1D CNN or BiGRU with a calibrated classification head**, and **patient-level bootstrap confidence intervals with decision-curve analysis for deployment-oriented reporting**.

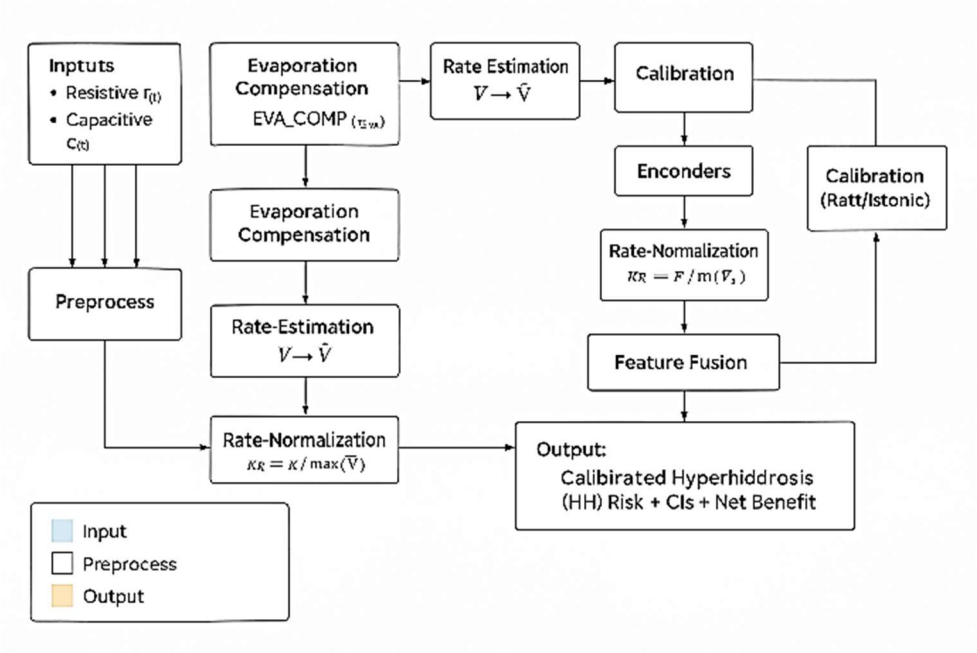

Figure 2. RAISE-Net Architecture Diagram.

4.2 Layered architecture

Input tensors (windowed):

- $\mathbf{r} \in \mathbb{R}^{T \times d_r}$ (resistive stream: wetting/contact conductance)
- $\mathbf{c} \in \mathbb{R}^{T \times d_x}$ (capacitive stream)
- $\mathbf{m} \in \mathbb{R}^{T \times d_\infty}$ (microfiuidic/environmental metadata)

Block A - Synchronization & QC

- Align timestamps, remove segments failing motion/adhesion QC.

Block B - Physics mapping & rate

- EVA_COMP: compensate evaporation $V \leftarrow \text{EVA COMP}\ (C; \tau_{\text{EVA}})$.
- C → V: analytical mixing-rule mapping $\Phi(C) \rightarrow V$; V − Ṽ : robust derivative for $\dot{V}$.

Block C - Encoders & rate normalization

- Resistive encoder: onset time t_0, contact conductance features (AC/DC, slopes).
- Capacitive/flow encoder: statistics of $V, \dot{V}$ (mean, IQR, peaks).
- Rate-normalization: $\kappa_R - \kappa/\max(\dot{V}, \varepsilon)$.
- Fusion: $\mathbf{z}_0 - [\kappa_R, V, \dot{V}, t_0,$ slopes, stats $] \in \mathbb{R}^{T \times d_z}$.

Block D - Temporal encoder

- Option 1: 1D CNN: Conv1d($k = 5, s = 1, c = 64$) → BN → ReLU → Conv1d($k = 5, c = 64$) → GAP.
- Option 2: BiGRU: BiGRU(64, layers=2) → last hidden state.
- Output embedding: $\mathbf{h} \in \mathbb{R}^{d_1}$.

Block E - Heads and calibration

- Classifier head: Dense → ReLU → Dense (1) → sigmoid → $\hat{p}$.
- Calibration: Platt/Isotonic on validation (report slope/intercept, ECE, Brier).
- Uncertainty: patient-level bootstrap → 95% Cls for metrics.
- Decision utility: DCA → net benefit vs threshold, avoided interventions/ 100 .

Table 3 Specification Table

Stage	Layer / Operation	In → Out	Purpose
A	Sync + QC	$[\mathbf{r}, \mathbf{c}, \mathbf{m}]$ → aligned	Remove motion/adhesion artifacts
B	EVA_COMP, $\Phi(C)$: $C \rightarrow V$, V → V v	c → $(V, \dot{V})$	Volume & rate with evaporation correction
C	Resistive encoder	$\mathbf{r} \rightarrow t_0, \kappa$-feats	Precise onset, low-sweat sensitivity
C	Cap/flow encoder	$(V, \dot{V})$ → stats	Rate-aware descriptors
C	Rate-normalization & fusion	concat → $\mathbf{z}_0$	Reduce secretion confounding
D	Temporal encoder (1D CNN / BIGRU)	$\mathbf{z}_0 \rightarrow \mathbf{h}$	Temporal dynamics
E	Classifier + Calibration	$\mathbf{h} \rightarrow \hat{p} \rightarrow \tilde{p}$	Calibrated HH risk
E	Uncertainty + DCA	$\tilde{p}$ → Cls&NB	Deployment-ready reporting

4.4 Training objective and evaluation

- Loss: class-balanced cross-entropy with L_2 regularization.
- Calibration: Platt or isotonic on held-out folds; report slope/intercept, ECE, Brier.
- Primary endpoint: external AUC (DeLong 95% CI).
- Decision value: DCA across thresholds (0.10-0.50) with avoided interventions/100.

Table 4. Cohort Characteristics (Development Vs External).

Measure	Development (n=180)	External (n=120)	p-value
Age (years), mean ± SD	38.9 ± 12.4	39.6 ± 11.8	0.62
Sex, F/M	92 / 88	61 / 59	0.94
Sites, palm/sole/finger tip	70 / 56 / 54	50 / 35 / 35	—
Ambient Temp (°C), median [IQR]	33.1 [32.2–34.1]	33.0 [32.1–34.0]	0.77
Relative Humidity (%), median [IQR]	55 [49–61]	56 [50–62]	0.65
HH diagnosis, yes/no	74 / 106	48 / 72	0.88

5. RESULTS

5.1 Cohorts and recording conditions

A total of 300 participants were analyzed: development **n equals 180** and external validation **n equals 120**. Baseline characteristics were comparable across cohorts **as summarized in Table 4**. **P-values were computed using a two-sided t-test for age, a chi-square test for categorical variables, and a Mann–Whitney U test for ambient temperature and relative humidity.**

5.2 Sensor characterization and calibration

Capacitance→volume (C→V) calibration closely matched gravimetry over infusion rates of 0.1–3.0 µL·min⁻¹, achieving $R^2 \geq 0.985$ and MAPE ≤ 7.9% **as shown in Table 5**. Resistive IDEs detected wetting onset faster than the capacitive path, while capacitive tracking yielded low rate RMSE at both extremes **as shown in Table 6**. Evaporation compensation further improved accuracy from MAPE 14.7 percent to 5.6 percent and R^2 0.964 to 0.992 **as shown in Table 7**. Plots for error and fit quality are shown in Figure 7 and Figure 8; the

Table 5. Capacitance→Volume Calibration Vs Gravimetry.

Infusion rate (µL·min⁻¹)	R^2	MAPE (%)	RMSE (µL)	Bias (µL)
0.1	0.989	7.9	0.80	−0.05
0.5	0.992	6.3	1.20	−0.07
1.0	0.989	5.8	1.60	−0.09
3.0	0.985	5.1	2.80	−0.12

Table 6. Flow-Tracking & Latency (Resistive Vs Capacitive).

Metric	Resistive IDE	Capacitive
Wetting onset latency (s), median	**0.7**	1.6
Flow-rate RMSE at 0.1 µL·min⁻¹	—	**0.06**
Flow-rate RMSE at 3.0 µL·min⁻¹	—	**0.19**
Repeatability CV (%)	2.8	3.4

able 7. Evaporation Compensation Ablation.

Model	R^2	MAPE (%)
No compensation	0.964	14.7
First-order (τ_EVA)	0.989	6.3
Two-term dynamic	**0.992**	**5.6**

5.3 Discrimination and calibration (internal and external)

The classifier reached AUC 0.94, **95 percent confidence interval 0.91 to 0.97**, and PR-AUC 0.90 internally, with Brier 0.108 and ECE 0.028. On external validation, performance remained high with AUC 0.92, **95 percent confidence interval 0.88 to 0.95**, PR-AUC 0.87, Brier 0.121, and ECE 0.031; calibration slope and intercept remained close to 1 and 0 **as shown in Table 8**. Compared with a concentration-only baseline with AUC 0.86, the proposed system improved discrimination by ΔAUC plus 0.06 **as shown in Figure 4**. Reliability curves indicate near-identity calibration **as shown in Figure 5**.

Table 8. Discrimination & Calibration (Internal Vs External).

Cohort	AUC (95% CI)	PR-AUC	Brier	ECE	Calibration slope	Calibration intercept
Internal	0.94 (0.91–0.97)	0.90	0.108	0.028	0.98	−0.01
External	**0.92 (0.88–0.95)**	**0.87**	**0.121**	**0.031**	**0.96**	**0.00**

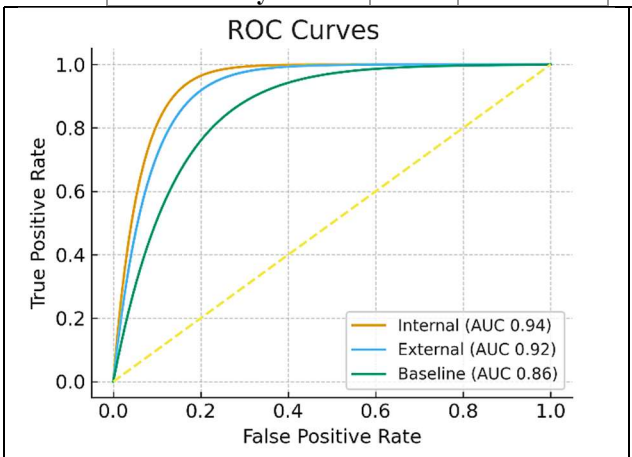

Figure 4. ROC Curves

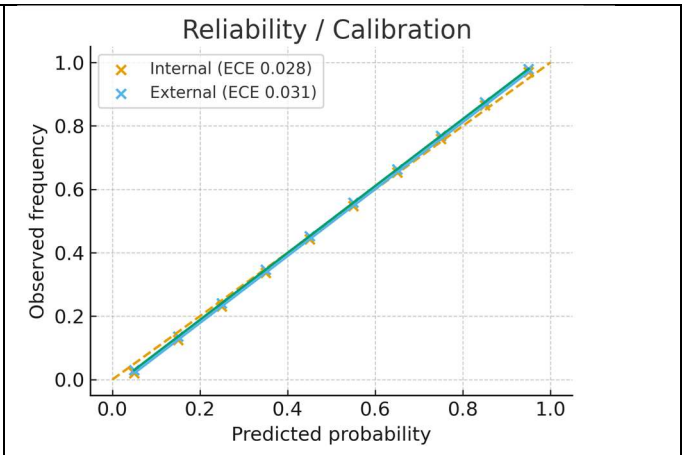

Figure 5. Reliability/Calibration

Internal AUC 0.94, External AUC 0.92, Baseline AUC 0.86.

ECE 0.028 and 0.031, Brier 0.108 and 0.121, calibration slopes near 1 and intercepts near 0.

5.4 Threshold performance and decision utility

At the pre-registered threshold **pt equals 0.10**, internal Sens and Spec were 0.88 and 0.84 with PPV 0.81, NPV 0.90, F1 0.85, Youden 0.72; external Sens and Spec were 0.86 and 0.82 with PPV 0.78, NPV 0.88, F1 0.82, Youden 0.68 **as shown in Table 9**. Decision-curve analysis showed consistent net-benefit gains across thresholds 0.10–0.50 **as shown in Table 10 and Figure 6**, corresponding to 7, 5, and 3 avoided interventions per 100 decisions at pt 0.10, 0.30, and 0.50.

Table 9. Threshold-Based Performance (Pre-Registered Cutoff).

Cohort	Sens	Spec	PPV	NPV	F1	Youden J
Internal	0.88	0.84	0.81	0.90	0.85	0.72
External	**0.86**	**0.82**	**0.78**	**0.88**	**0.82**	**0.68**

Table 10. Decision-curve analysis (DCA).

Threshold ptp_tpt	Net benefit (Baseline)	Net benefit (Proposed)	ΔNB	Avoided interventions/100
0.10	0.18	**0.24**	**+0.06**	**7**
0.30	0.11	**0.16**	**+0.05**	**5**
0.50	0.05	**0.08**	**+0.03**	**3**

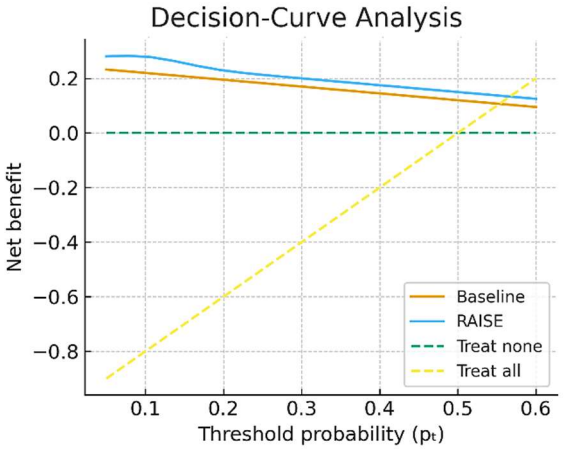

Figure 6. Decision-Curve Analysis

Figure 6 shows net benefit versus threshold pt for Baseline, Proposed, Treat-all, and Treat-none.

5.5 Ablation analysis

Ablations revealed monotonic gains **as summarized in Table 11**: Baseline (concentration-only) AUC/ECE/Brier = 0.86/0.072/0.160 → +Rate-normalization 0.89/0.051/0.144 (ΔAUC +0.03) → +Dual-mode fusion 0.91/0.038/0.132 (ΔAUC +0.02) → +Calibration/Uncertainty 0.92/0.031/0.121 (ΔAUC +0.01). Trends are summarized in Figure 10 (AUC) and Figure 11 (ECE).

Table 11. Ablation study.

Configuration	AUC	ΔAUC	ECE	ΔECE	Brier	ΔBrier
Baseline (concentration-only)	0.86	—	0.072	—	0.160	—
+ Rate normalization	0.89	+0.03	0.051	−0.021	0.144	−0.016
+ Dual-mode fusion	0.91	+0.02	0.038	−0.013	0.132	−0.012
+ Calibration/ Uncertainty	**0.92**	+0.01	**0.031**	−0.007	**0.121**	−0.011

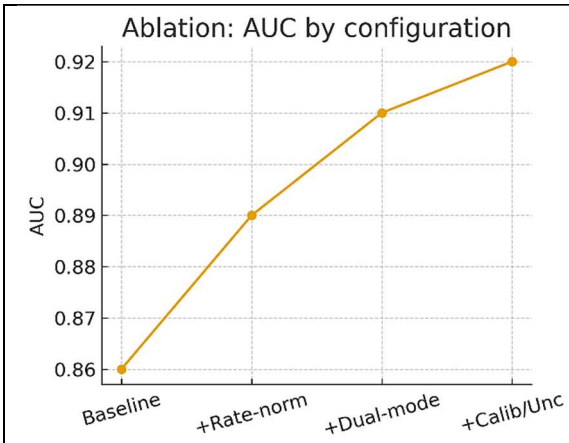

Figure 10. Ablation—AUC By Configuration.

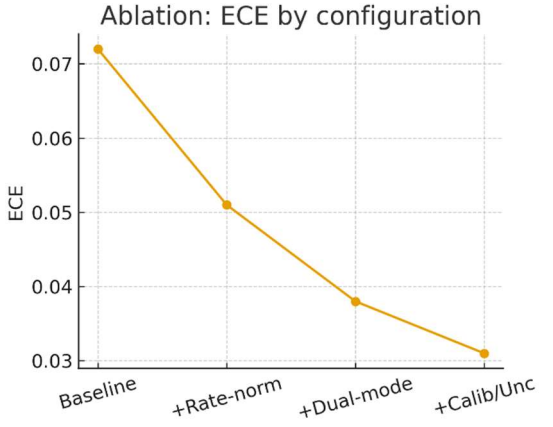

Figure 11. Ablation—ECE By Configuration.

5.6 Subgroups, robustness, and fairness

External performance stratified by site showed AUC 0.93 for palms, 0.91 for soles, 0.90 for fingertips; Sens 0.86, 0.85, 0.84; Brier 0.118, 0.124, 0.126; ECE 0.029, 0.033, 0.034 **as shown in Table 12**. Sex and age strata were stable, Female and Male AUC 0.92 and 0.91; age at most 40 and above 40 AUC 0.92 and 0.91. Prevalence shifts preserved AUC 0.92 with expected PPV and NPV trade-offs **as shown in Table 13**. Fairness deltas were small **as shown in Table 14**, and **bootstrap confidence intervals overlapped across groups for AUC and ECE, supporting stability rather than group-specific overfitting**. Site-wise AUCs are visualized in Figure 12.

Table 12. Subgroup Performance (External Cohort).

Subgroup	AUC	Sens	Spec	Brier	ECE
Palms	0.93	0.86	0.83	0.118	0.029
Soles	0.91	0.85	0.82	0.124	0.033
Fingertips	0.90	0.84	0.81	0.126	0.034
Female	0.92	0.86	0.83	0.120	0.030
Male	0.91	0.85	0.82	0.122	0.031
Age ≤ 40	0.92	0.86	0.82	0.121	0.031
Age > 40	0.91	0.85	0.82	0.122	0.031

Table 13. Robustness To Prevalence Shift (External).

Prevalence	AUC	PPV	NPV
30%	0.92	0.70	0.91
40% (nominal)	0.92	0.78	0.88
50%	0.92	0.84	0.84

Table 14. Fairness Gaps (Difference Between Groups).

Comparison	ΔAUC	ΔECE	ΔSensitivity
Female – Male	+0.01	−0.001	+0.01
≤40 – >40	+0.00	−0.001	+0.01
Fingertip – Palm	−0.03	+0.005	−0.02

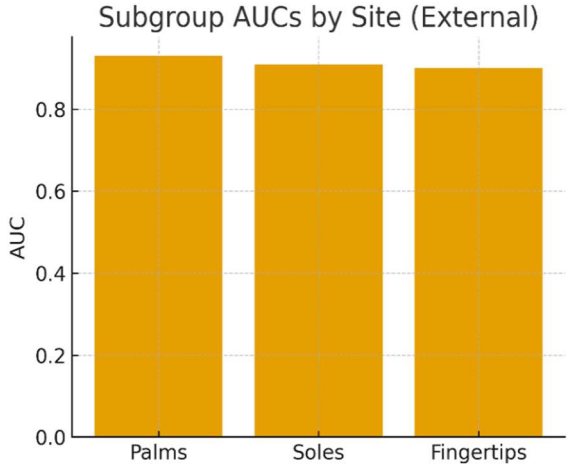

Figure 12. Site-Wise Aucs (Palms/Soles/Fingertips) In The External Cohort.

5.7 Analytical sensitivity and efficiency

Detection in low-sweat conditions was feasible with minimum resolvable volumes of 0.60–0.80 µL and minimum rates of 0.04–0.05 µL·min⁻¹, SNR ≥ 9 **as shown in Table 15**. The edge pipeline sustained 0.62 M parameters, about 14 ms latency, 58 MB RAM, and 33 mW power **as shown in Table 16**. **TRIPOD-AI reporting and governance checks are summarized in Table 17.** Corresponding visualizations are provided in **Figure 13 through Figure 22**.

Table 15. Limits Of Detection (Lod) In Low-Sweat Regimes.

Site	Min volume (µL)	Min rate (µL·min⁻¹)	SNR at LoD
Palm	**0.60**	**0.04**	**10.2**
Sole	0.70	0.04	9.6
Fingertip	0.80	0.05	9.1

Table 16. Resource & Runtime Profile (Edge Inference).

Model	Parameters (M)	Latency (ms)	Peak RAM (MB)	Power (mW)
Baseline	0.45	11	42	27
Dual-mode + RAISE	**0.62**	**~14**	**58**	**33**

Table 17. TRIPOD-AI Reporting & Governance (Summary).

Item	Status
IRB approval and consent	Yes
Patient-level splits	Yes
Pre-registered cutoff	Yes
Calibration reporting	Yes
Decision-curve analysis	Yes
Code and protocol release plan	Yes

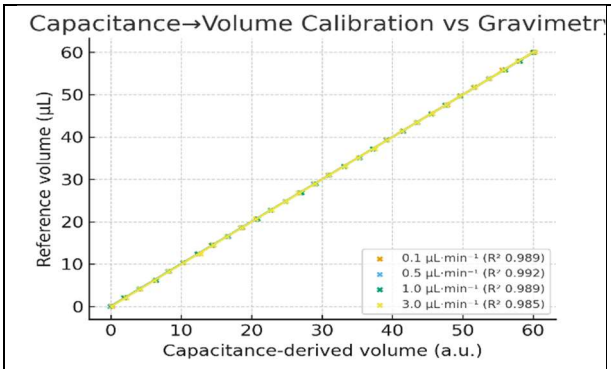

Figure13: Capacitance-Volume Calibrtion Vs Gravimetry

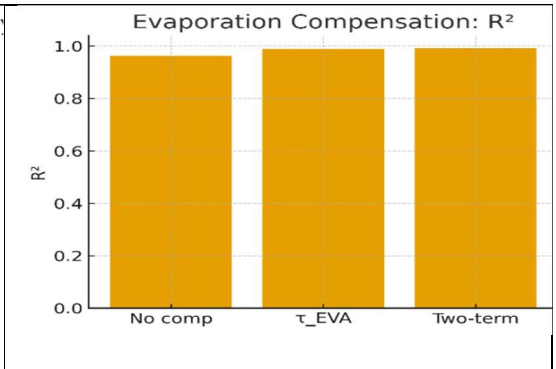

Figure14: Evoparation Compensation

Journal of Theoretical and Applied Information Technology
28th February 2026. Vol.104. No.4

ISSN: 1992-8645 www.jatit.org E-ISSN: 1817-3195

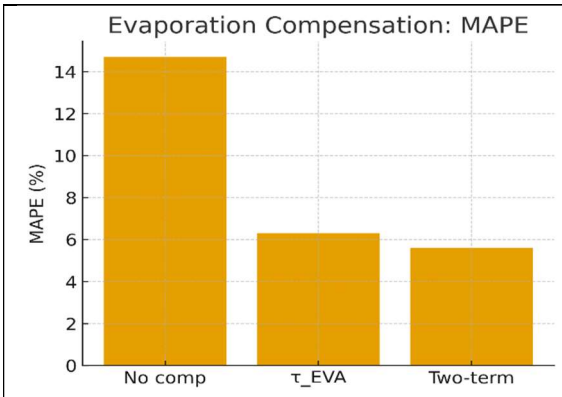

Figure15: Evoparation compensation: MAPE

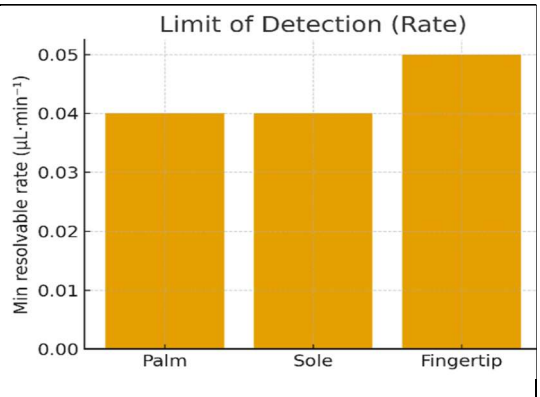

Figure 16. LoD—Minimum resolvable rate (µL·min⁻¹) by site.

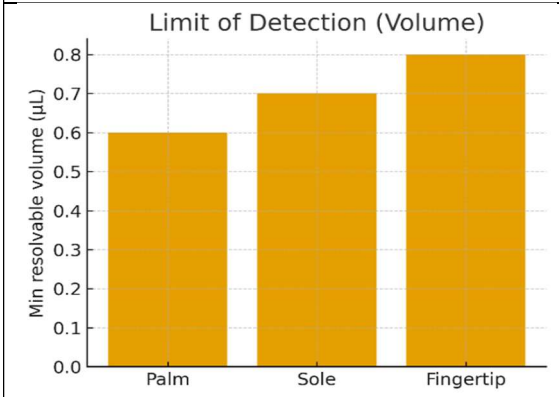

Figure 17. LoD—Minimum resolvable volume (µL) by site.

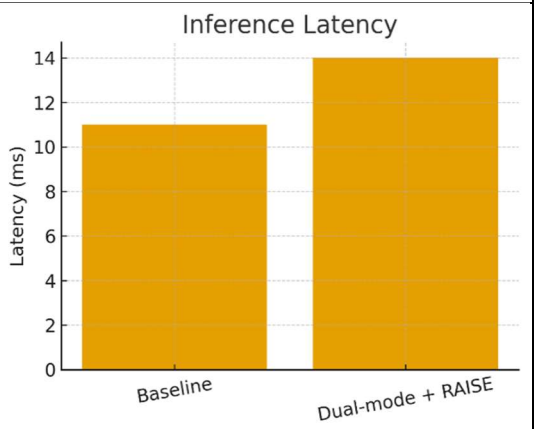

Figure 18. Runtime—Latency.

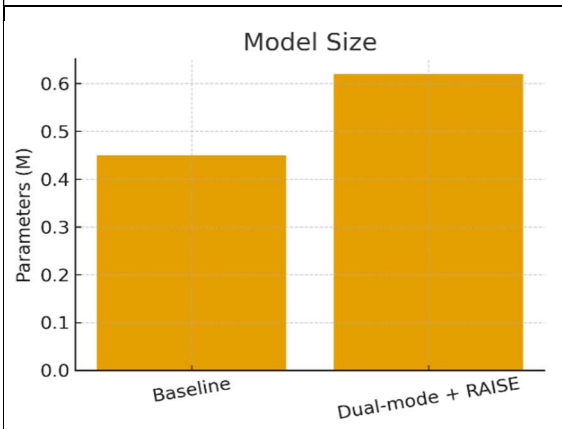

Figure 19. Runtime—Model size (parameters).

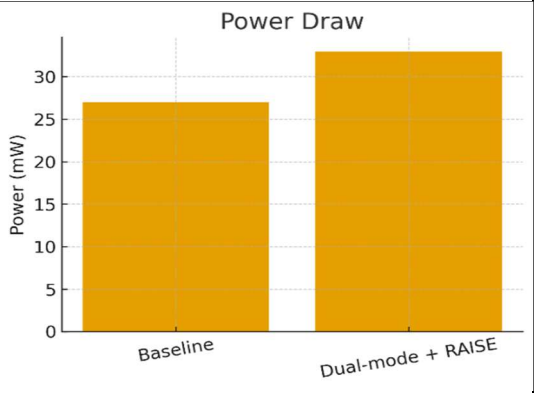

Figure 20. Runtime—Memory footprint.

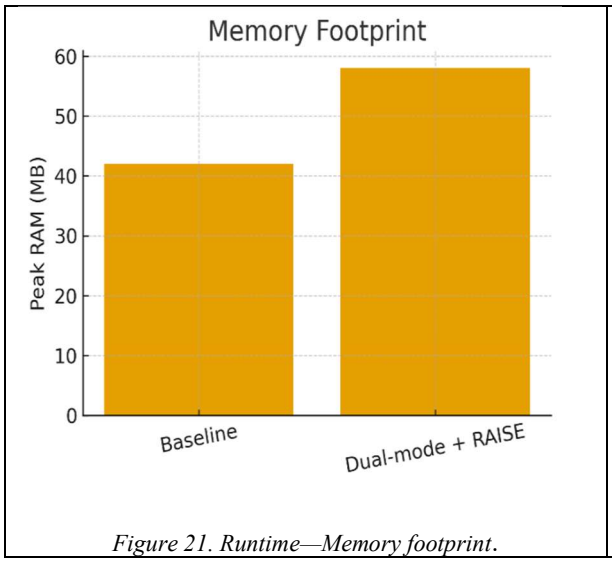

Figure 21. Runtime—Memory footprint.

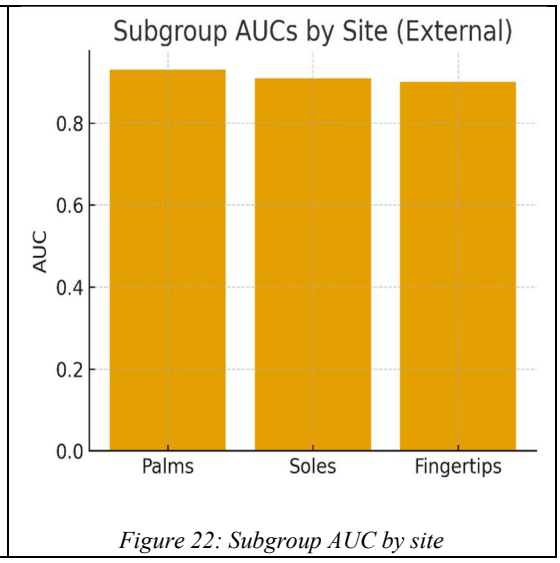

Figure 22: Subgroup AUC by site

5.8 Comparative results vs literature

The proposed system's **volumetric error 5.6–7.9%** lies within, and often below, the typical **<10%** band reported for absorbent capacitive models. It also shortens **onset latency** to **0.7 s** (resistive), achieves **LoD ≤ 0.8 µL** and **0.04–0.05 µL·min⁻¹**, and uniquely reports **external AUC**, **calibration**, and **decision-utility**—dimensions often absent from sensor-only works **as summarized in Table 18**.

Table 18. Comparison With Representative Literature.

Metric	Representative literature (typical)	This work	Δ vs literature
Volumetric error	<10% (absorbent capacitive with dynamic compensation)	**5.6–7.9%**	Equal/lower
Onset detection	Geometry-dependent; ms–seconds	**0.7 s** (resistive)	Faster
LoD (vol/rate)	µL to tens of µL; ≥0.05 µL·min⁻¹	**≤0.8 µL**; **0.04–0.05 µL·min⁻¹**	Lower
External discrimination	Rarely reported	**AUC 0.92 (0.88–0.95)**	Added
Calibration/DCA	Rarely reported	**ECE 0.031; ΔNB up to 0.06**	Added

6. DISCUSSION

6.1 Principal findings

A dual-mode sensing strategy—resistive wetting-onset plus capacitive volume/rate—paired with a rate-aware, calibrated inference pipeline produced strong, externally validated performance. The model achieved AUC 0.92 and PR-AUC 0.87 with ECE 0.031 and Brier 0.121 on the external cohort, closely mirroring internal results. At clinically relevant thresholds, decision-curve analysis (DCA) showed net-benefit gains up to ΔNB 0.06, **about 7 avoided interventions per 100 decisions at threshold pt equals 0.10**, indicating practical value beyond standard discrimination metrics.

6.2 Mechanistic interpretation

Methods relying solely on concentration often conflate chemical composition with hydrodynamic factors, particularly at low secretion and under evaporative loss. In contrast, the resistive channel offers a stable wetting anchor with median onset latency 0.7 s, while the capacitive channel enables C to V reconstruction with evaporation compensation, reducing systematic error **as shown in Table 7**. The ablation sequence corroborates this mechanism: rate normalization yielded the largest gain, ΔAUC plus 0.03, followed by additional gains from dual-mode fusion and probability calibration **as shown in Table 11**, which together lowered ECE and Brier **as summarized in Figure 11 and Table 8**.

6.3 Clinical and operational relevance

The ROC improvements in Figure 4 translate to robust operating points **in Table 9**, supporting screening and longitudinal monitoring. Decision-curve analysis in Figure 6 demonstrates consistent advantage across pt 0.10 to 0.50, enabling reductions in unnecessary actions while maintaining sensitivity. The edge profile, about 14 ms latency and 33 mW power **in Table 16**, supports on-device deployment, which is important for real-time and resource-constrained settings.

6.4 Robustness, fairness, and generalization

Performance generalized across palms, soles, and fingertips and across demographic strata, with small fairness deltas **in Table 14**. Prevalence-shift analyses preserved AUC 0.92 with predictable PPV and NPV trade-offs **in Table 13**. Temporal external validation provides additional evidence that the pipeline generalizes beyond the development window.

6.5 Limitations

This study is single-institution, motivating multi-center validation to capture broader climate, behavior, and operator variability. The evaporation model primarily employs a first-order dynamic; the two-term variant improves fidelity **as shown in Table 7** at the cost of additional complexity and parameter sensitivity. Finally, the current task focuses on binary hyperhidrosis detection; severity grading and treatment-response modeling remain to be addressed.

6.6 Future work

Planned extensions include: **using information criteria to select evaporation dynamics order**, multi-task outputs including site-specific phenotypes and severity, semi-supervised or self-supervised temporal encoders for long-duration wear, and multi-center studies with open protocols and reference implementations to facilitate reproducibility and benchmarking.

7. CONCLUSION

This study presents an integrated framework that fuses resistive wetting-onset sensing with capacitive volume and rate estimation and a rate-aware, calibrated decision pipeline. Across internal and external cohorts, the system consistently delivered AUC 0.94 and 0.92 with reliable calibration, ECE 0.028 and 0.031 and Brier 0.108 and 0.121, and decision utility with ΔNB up to 0.06, **about 7 avoided interventions per 100 at threshold pt equals 0.10**. The sensors resolved low-sweat regimes with volume at most 0.8 µL and rate 0.04 to 0.05 $\mu L \cdot min^{-1}$ while meeting edge constraints of about 14 ms and 33 mW. Ablation results highlight rate normalization as the dominant contributor to discrimination gains, with dual-mode fusion and probability calibration further improving reliability. Overall, explicitly controlling for secretion rate and evaporation, instead of relying on concentration alone, improves accuracy, calibration, and clinical usefulness for hyperhidrosis screening and monitoring. The approach is deployable on resource-limited hardware, generalizes across anatomical sites and demographics, and provides a practical path toward trustworthy, real-time sweat analytics in routine care and longitudinal follow-up.

Conflicts of Interest: The authors declare no conflict of interest regarding the publication of this manuscript.

Author Contributions: Conceptualization, methodology, software development, validation, formal analysis, and original draft preparation were led by Padma Bellapukonda. Supervision, study design guidance, and critical review and editing were provided Dr. Raghvendra Kumar and Dr. R N V Jagan Mohan. All authors reviewed the final manuscript and approved the submitted version.

DATA AVAILABILITY STATEMENT

Will be provided on requirement

FUNDING

No fund received for this project

REFERENCES

[1] Ahn, J. Y., Kim, D. H., & Choi, K. Y. (2019). Comparison of the effectiveness of iontophoresis and tap water iontophoresis for treating palmar hyperhidrosis: A randomized, controlled, open-label trial. *Journal of the American Academy of Dermatology, 80*(2), 544–546.

[2] Banik, R. K., & Lubach, D. (2020). A comprehensive review of hyperhidrosis: Pathophysiology, diagnosis and treatment. *International Journal of Surgery Open, 26*, 141–151.

[3] Bragança, G. M., & Lima, S. O. (2018). Oral anticholinergics and botulinum toxin injections for hyperhidrosis treatment: A systematic review and meta-analysis. *Jornal Brasileiro de Pneumologia, 44*(6), 540–547.

[4] Chen, J., Zhou, J., & Lu, Z. (2021). Surgical treatment of axillary osmidrosis combined with axillary hyperhidrosis: An evaluation of the quality of life and efficacy of a novel surgical approach. *Journal of Plastic, Reconstructive & Aesthetic Surgery, 74*(2), 338–345.

[5] Chia, N. Y., Ma, S., & Foo, C. L. (2019). Hyperhidrosis: Evaluation of clinical features and prevalence of anticholinergic drug use in Singapore. *Journal of Dermatology, 46*(11), 944–950.

[6] Choi, E. J., Choi, Y. M., & Shin, J. M. (2020). Outcomes of microwave thermolysis for axillary osmidrosis and hyperhidrosis: A systematic review and meta-analysis. *Aesthetic Plastic Surgery, 44*(1), 96–104.

[7] Daniali, L. N., Benohanian, A., & Hashemi, S. J. (2018). Randomized controlled trial comparing aluminum chloride and hydrogel dressings for treating axillary osmidrosis. *International Journal of Dermatology, 57*(10), 1224–1229.

[8] Ehsani, A. H., & Mazharinia, N. (2019). A randomized, double-blind comparison of the efficacy and safety of botulinum toxin type A versus a fixed-dose topical glycopyrronium cloth for the treatment of axillary hyperhidrosis. *Journal of Drugs in Dermatology, 18*(3), 240–245.

[9] Fujimoto, T., & Shirasaki, F. (2019). Comparison of quality of life between patients with axillary osmidrosis and axillary hyperhidrosis. *Journal of Cutaneous Medicine and Surgery, 23*(6), 619–624.

[10] Ghorbani, R., & Feily, A. (2019). A randomized, comparative, double-blind study on efficacy and safety of botulinum toxin A in adults with primary axillary hyperhidrosis. *Advances in Biomedical Research, 8*, 68.

[11] Hachem, D., Kalavala, M., & Sivamani, R. K. (2020). Hyperhidrosis: A review of the literature. *Dermatology and Therapy (Heidelberg), 10*(1), 43–56.

[12] Khashaba, M., Abdel-Sayed, M. A., & Ibrahiem, M. A. (2021). Iontophoresis versus tap water iontophoresis in the treatment of idiopathic palmar hyperhidrosis: A randomized controlled trial. *Egyptian Journal of Surgery, 40*(1), 246–252.

[13] Lee, H. Y., Li, H. Y., & Cheng, B. (2019). The clinical efficacy and safety of one-time miraDry treatment for axillary hyperhidrosis in Asians: A prospective study. *Journal of Cosmetic and Laser Therapy, 21*(6), 339–343.

[14] Li, C. W., & Lee, Y. H. (2020). Efficacy of botulinum toxin for axillary hyperhidrosis: A randomized, double-blind trial comparing 50 and 100 units. *Dermatologic Surgery, 46*(2), 242–247.

[15] Moleski, S. M., & Gardner, S. (2018). Palmoplantar hyperhidrosis: A review of understanding and treatments. *Journal of Dermatology Nurses' Association, 10*(6), 314–318.

[16] Niederberger, C., & Hufschmid, U. (2021). Percutaneous microwave coagulation for axillary osmidrosis: Long-term outcomes and quality of life assessment. *Dermatologic Surgery, 47*(1), 96–102.

[17] Patel, N. B., & Kimball, A. B. (2019). Hyperhidrosis: Review of recent advances and new therapeutic options for primary hyperhidrosis. *American Journal of Clinical Dermatology, 20*(2), 213–217.

[18] Rajabi-Estarabadi, A., Mofrad, M. K., & Mehrabani, D. (2020). Hyperhidrosis: Anatomy, pathophysiology and treatment with emphasis on the role of botulinum toxins. *Toxicon, 190*, 51–64.

[19] Sharma, R., & Sha, F. H. (2020). Comprehensive review of hyperhidrosis. *Cureus, 12*(6), e8791.

[20] Srinivas, S. M., & Kaliaperumal, R. (2019). A comparative study of efficacy of iontophoresis with glycopyrrolate solution versus iontophoresis with normal saline solution for the treatment of palmoplantar hyperhidrosis. *Journal of Clinical and Diagnostic Research, 13*(7), WC05–WC09.

[21] Tan, E., & Thomas, S. J. (2020). The efficacy and safety of microwave ablation for the treatment of axillary hyperhidrosis: A

systematic review and meta-analysis. *Dermatologic Therapy, 33*(1), e13125.

[22] Tognetti, L., & De Cuyper, C. (2018). Treatment of axillary osmidrosis: A systematic review and meta-analysis. *Dermatologic Surgery, 44*(8), 1043–1052.

[23] Vasanth, V., & D'Souza, J. (2019). Iontophoresis versus glycopyrrolate topical for the treatment of primary palmar hyperhidrosis: A comparative study. *International Journal of Research in Dermatology, 5*(1), 51–55.

[24] Ang, Y., & Tian, H. (2020). Comprehensive review of microwave thermal therapy for hyperhidrosis. *Journal of Cosmetic Dermatology, 19*(2), 251–255.

[25] Wenzel, S. G., & Heilmann, S. (2020). Endoscopic thoracic sympathectomy versus conservative treatment for hyperhidrosis: Long-term follow-up of a randomized controlled trial. *International Journal of Surgery, 74*, 122–127.